The Planetary Science Journal, 5:229 (11pp), 2024 October https://doi.org/10.3847/PSJ/ad72ee

Simulated Solar-wind-induced Space Weathering of Olivine Powders: Spectral Alterations in the Ultraviolet, Visible, and Near-infrared

Camilo Jaramillo-Correa[1,2,3], Neil C. Pearson[4], Deborah Domingue[4], Daniel W. Savin[5], Roger N. Clark[4], Faith Vilas[4], and Amanda R. Hendrix[4]
[1] Department of Chemical and Biological Engineering, Princeton University, Princeton, NJ, 08544, USA; cjaramillo@princeton.edu
[2] Ken and Mary Alice Lindquist Department of Nuclear Engineering, The Pennsylvania State University, University Park, PA, 16802, USA
[3] Materials Research Laboratory, University of Illinois at Urbana-Champaign, Urbana, IL, 61801, USA
[4] Planetary Science Institute, Tucson, AZ, 85719, USA
[5] Columbia Astrophysics Laboratory, Columbia University, New York, NY, 10027, USA
Received 2024 May 13; revised 2024 August 9; accepted 2024 August 18; published 2024 October 17

Abstract

Bombardment by solar wind ions is one of the main drivers of space weathering on airless bodies. Here, we simulate the solar-wind-driven spectral alteration of loosely packed olivine powders by irradiation with 1.2 keV helium ions (He^+). We measured the reflectance spectra of the olivine powder in the ultraviolet–visible–near-infrared (UV–Vis–NIR) wavelength range (0.2–2 μm) as a function of ion fluence. In the Vis–NIR range, we observed spectral darkening, absorption band shallowing, and spectral reddening, in agreement with lunar-style space weathering and previous laboratory studies. In the UV–Vis, spectral darkening was also observed. However, a spectral bluing took place at wavelengths below 400 nm. As the simulated space weathering progressed, the spectral slopes shifted from steep-UV/shallow-NIR slopes to shallow-UV/steep-NIR slopes. Moreover, the change in the UV slope was almost 10 times larger than in the NIR, supporting the hypothesis that the UV spectral slope could be an earlier indicator of space weathering.

Unified Astronomy Thesaurus concepts: Asteroid surfaces (2209); Solar wind (1534); Infrared spectroscopy (2285); Ultraviolet spectroscopy (2284); Planetary science (1255); Experimental techniques (2078)

Materials only available in the online version of record: Data-Behind Figures

1. Introduction

The study of the composition and makeup of the surface of airless bodies in our solar system is largely derived from remote reflectance spectroscopy observations. Important information such as mineralogy and surface characteristics (porosity and particle size distribution) can be inferred from the reflectance spectra in the ultraviolet, visible, and near-infrared (UV–Vis–NIR) wavelength ranges (C. M. Pieters & L. A. McFadden 1994; E. A. Cloutis et al. 2018). The surfaces of airless bodies are directly exposed to micrometeorite impacts and particle and electromagnetic radiation, which gradually alter their physicochemical properties, in a group of processes that are collectively known as space weathering (B. Hapke 2001). Space weathering affects the top few nano- to millimeters of the surface, altering the mineralogical characteristics from their pristine or bulk state. UV-to-NIR spectral observations are sensitive to a depth that is within this altered surface layer. Thus, space weathering can affect the spectral characteristics of airless bodies and make the interpretation of remote reflectance spectroscopy observations challenging (C. R. Chapman 2004).

Most of our understanding of space weathering has come from the analysis of lunar samples and, more recently, asteroid samples (T. Noguchi et al. 2011, 2022; D. L. Domingue et al. 2014). In general, space weathering processes produce nanoscale amorphous rims on grain surfaces that contain nanoscale inclusions, ranging in composition from metallic iron (npFe) to iron–nickel (npFeNi) or iron sulfide (npFeS). These inclusions have been observed in lunar samples (L. P. Keller & D. S. McKay 1993, 1997; S. J. Wentworth et al. 1999; L. P. Keller et al. 2000; C. M. Pieters et al. 2000; L. Gu et al. 2018) and asteroid samples (T. Noguchi et al. 2011, 2012, 2014, 2022; T. Matsumoto et al. 2020; L. C. Chaves & M. S. Thompson 2022). It is the amorphization of the rims and the inclusions within them that affect the spectral properties. Similar mineral alterations have been observed in laboratory simulations of space weathering (C. A. Dukes et al. 1999; P. Carrez et al. 2002; M. J. Loeffler et al. 2009; J. M. Young et al. 2019).

Since the early reports of evidence for space weathering on the Moon (B. Hapke 1973), the ways in which space weathering affects spectra in the Vis–NIR wavelength range have been studied extensively. Three spectral effects have been identified: (1) spectral darkening, (2) shallowing of absorption bands, and (3) spectral reddening (increasing reflectance with increasing wavelength) (B. Hapke 2001; Clark et al. 2002; D. L. Domingue et al. 2014; C. M. Pieters & S. K. Noble 2016). The first two effects are diagnostic of space weathering. However, the changes in the spectral slope have been shown to be controlled by the size of submicron-scale iron (smFe) domains produced by space weathering. Micron-scale phase iron domains (mpFe) seem to have no effect on the spectral slope, while the npFe fraction produces the spectral reddening (S. K. Noble et al. 2007; D. T. Blewett et al. 2021).

Laboratory and observational studies of space weathering have largely focused on the Vis–NIR wavelength range. S-class asteroids have been found to demonstrate lunar-like space

weathering effects (C. R. Chapman 1999; B. Hapke 2001). In the UV spectral region, the weathering effects on S-class asteroids are the opposite of those seen in the Vis–NIR: spectral bluing is observed instead of the spectral reddening that is characteristic of the NIR range (A. R. Hendrix & F. Vilas 2006). The slope effects are also dependent on the smFe size range (D. T. Blewett et al. 2021). Moreover, asteroid studies indicate that the UV region is more sensitive to space weathering effects, as the bluing effects can occur in less mature regolith, before the reddening occurs in the NIR region (A. R. Hendrix & F. Vilas 2006; F. Vilas & A. R. Hendrix 2015).

Laboratory simulations can be used as a tool to understand the physicochemical alteration incurred by space weathering and its effects on various minerals and their spectral properties. These simulations have largely focused on micrometeoroid impact and solar wind ions, which are widely considered to be the main drivers of space weathering (C. J. Bennett et al. 2013). Other contributors include photons and cosmic rays (C. M. Pieters & S. K. Noble 2016). Thus, laboratory simulations have mostly focused on reproducing weathering processes by micrometeoroid impact using laser irradiation to emulate the energy deposition (J. J. Gillis-Davis et al. 2017; Y. Yang et al. 2017; K. Fiege et al. 2019; M. S. Thompson et al. 2020), by solar wind ions (C. A. Dukes et al. 1999; K. Demyk et al. 2001; G. Strazzulla et al. 2005; M. J. Loeffler et al. 2009; D. J. Burke et al. 2011), or a combination of the two (M. J. Loeffler et al. 2008). The population of solar wind ions consists of ∼95% hydrogen and ∼5% helium, with heavier elements present in trace amounts. The solar wind properties are highly dynamic, varying in both space and time. At 1 au in the ecliptic plane, the solar wind has an average ion density of $\sim 8\,\mathrm{cm}^{-3}$, whereas its flow speed is typically in the 300–700 $\mathrm{km\,s}^{-1}$ range, with an average of 468 $\mathrm{km\,s}^{-1}$ (B. E. Goldstein 1998; J. T. Gosling 2014). This corresponds to about 1 keV amu^{-1}. Despite the highly dynamic nature of the solar wind, the 1 keV amu^{-1} figure has become useful for simulation studies. Laboratory simulations have largely focused on 4 keV He^{+} irradiation for two main reasons: (1) simulated space weathering occurs more rapidly with He irradiation than with H irradiation, which enables measurements to be performed on timescales that are achievable in the laboratory, and (2) it is challenging to generate He^{++} beams with sufficiently large currents to induce space-weathering-like effects in realistic timelines in a laboratory setting (C. A. Dukes et al. 1999; P. Vernazza et al. 2013; R. Brunetto et al. 2014; L. P. Keller et al. 2015b; C. Lantz et al. 2017; D. L. Laczniak et al. 2019, 2021).

In this work, we report the spectral alteration of loosely packed olivine powders—$(Mg,Fe)_2SiO_4$—irradiated with helium ions (He^{+}) to simulate space weathering effects due to solar-wind-like ion bombardment. Specifically, we used in situ reflectance spectroscopy, covering the UV–Vis–NIR wavelength range, testing the hypothesis that the two wavelength regimes (UV–Vis and Vis–NIR) show a different response and are sensitive to different stages in the weathering process.

The irradiations were carried out using San Carlos olivine as a target. Olivine is a common mineral found on the lunar surface and S-type asteroids (C. R. Chapman 1996; P. G. Lucey 2004; E. A. Cloutis et al. 2015). San Carlos olivine has also been extensively characterized; thus, our Vis–NIR measurements could be compared with similar published studies to further validate our approach. Although minor variations in composition have been observed, generally speaking, San Carlos olivine is magnesium-rich, with a forsterite content of about 90% (S. Lambart et al. 2022). Even in magnesium-rich olivine, most of the spectral features can be associated with iron (E. A. Cloutis et al. 2008). This mineral is also representative of S-type asteroids (M. J. Gaffey et al. 1993; C. R. Chapman 1996), is readily available, and provides a link to interpret the effects of space weathering on these and similarly low-iron (but not iron-free) planetary body surfaces.

The olivine sample was ground down into fine powder (<25 μm) to mimic the finest fraction of loose regolith and to study how ion irradiation alters the spectral characteristics of a loosely packed mineral powder. The grain size was chosen to be within the predicted grain size distribution of regolith on the surface of airless bodies (tens to a few hundred μm; A. Dollfus et al. 1989; Clark et al. 2002; S. D. Price 2004; M. A. Barucci et al. 2019).

The remainder of this paper is organized as follows. In Section 2, we describe the procedure followed to prepare the olivine powders and the setup used to irradiate and characterize the samples. In Section 3, we present the spectral characteristics of the ion-irradiated olivine. In Section 4, we discuss and compare the way each wavelength range (UV, Vis, and NIR) is altered by the ion irradiation and how our results compare to other studies. We close in Section 5 with some concluding remarks about our results.

2. Experimental Setup

The ion irradiation and mineral characterization were carried out in the Ion-Gas-Neutral Interactions with Surfaces (IGNIS) facility, a high-vacuum surface science facility located at the University of Illinois at Urbana-Champaign (E. Lang et al. 2017; P. Luo et al. 2020). Olivine powders were exposed to helium ion beams, and reflectance spectra of the irradiated mineral were collected in situ.

For this work, magnesium-rich San Carlos olivine was used as the target mineral. Coarse particles (>1 mm) were handpicked from Peridot Mesa in San Carlos, AZ. Olivine from this location has been previously characterized (S. Lambart et al. 2022). The particles were manually ground using a porcelain mortar and pestle. The ground material was sieved using a 25 μm mesh sieve. Approximately 0.5 g of the <25 μm olivine powder was collected into a sample cup (cylindrical shape, 17 mm wide and 3 mm deep) for irradiation and characterization. This corresponds to a sample density (ρ_{sample}) of 0.7 $\mathrm{g\,cm}^{-3}$. Considering an olivine true density (ρ_{true}) of 3.35 $\mathrm{g\,cm}^{-3}$, the sample porosity is approximately

$$\text{Porosity } \% = \left(1 - \frac{\rho_{\mathrm{sample}}}{\rho_{\mathrm{true}}}\right) \times 100 \approx 78. \quad (1)$$

The sample cup was lightly tapped to obtain a relatively flat, loosely packed sample surface, but the powders were not mechanically pressed.

The entire sample preparation procedure was carried out inside a glovebox filled with a nitrogen environment to prevent sample contamination by exposure to air. During the sample grinding, a Workstation ionizer (SPI Westek) and a Zerostat 3 anti-static gun (Milty) were used to minimize static inside the glovebox and reduce the powder clumping due to static. While the sample was processed, the water and oxygen contents inside the glovebox were <0.55 ppm and <0.12 ppm,

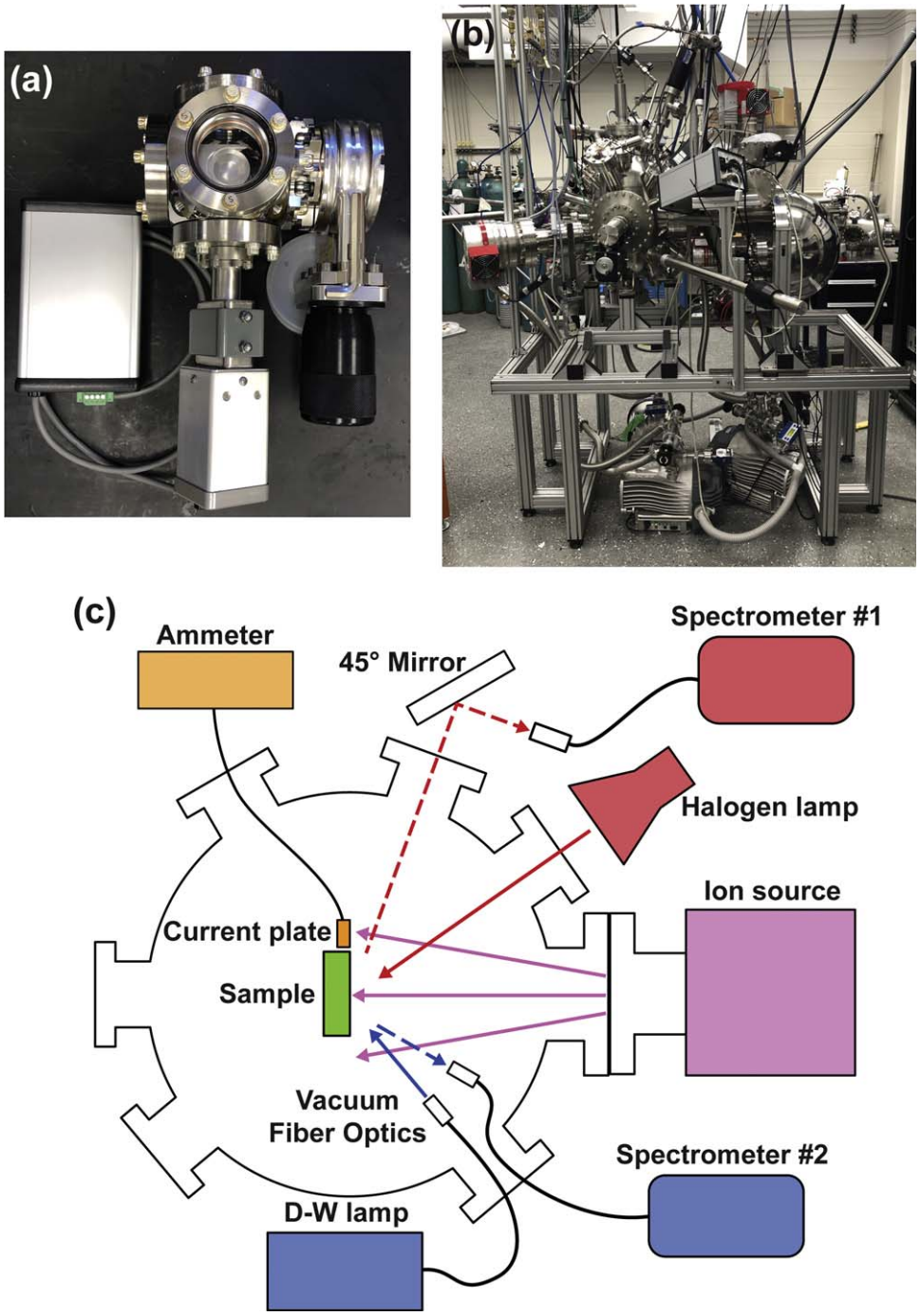

Figure 1. Experimental setup used for the preparation and irradiation of olivine powder with in situ UV–Vis–NIR reflectance spectroscopy. (a) Vacuum suitcase used to transport the samples from the glovebox to the experimental facility. (b) The IGNIS facility, where the irradiation and spectra collection were carried out. (c) Schematic of the IGNIS main chamber showing the main components used for this work. Components of the Vis–NIR reflectance setup are shown in red, where the solid and dashed line represent the incident and reflected light, respectively. The components shown in blue correspond to the UV–Vis reflectance setup, where the solid and dashed line represent the incident and reflected light, respectively. The solid pink arrows represent the ion beam.

respectively. Doing the preparation in a glovebox enabled us to generate particles with fresh faces from deep inside the coarse particles (faces that had no exposure to air). To illustrate this, turning a spherical grain with 1 mm diameter into powder with a particle size of 25 μm would increase the surface area by a factor of 40, and the fresh faces would account for ~97% of the total surface area.

While inside the glovebox, the sample cup was loaded into an environmental suitcase (Figure 1(a)), which was then sealed to retain the nitrogen background. Next, the suitcase was removed from the glovebox and immediately transported to the experimental stage (IGNIS; Figure 1(b)) without exposing it to air. This enabled us to maintain the sample in an inert environment to prevent chemical alteration of the mineral surface due to interactions with reactive species in air and adsorption of adventitious carbon.

The vacuum suitcase was mounted on a dedicated interfacing port on the load-lock chamber on IGNIS, which was backfilled

Table 1
Summary of the Ion Irradiation Carried Out on the Olivine Loose Powder Sample to Simulate Solar Wind Ion-driven Space Weathering

Step	Fluence (ions cm^{-2}) (Increase)	Fluence (ions cm^{-2}) (Cumulative)
00	...	0
01	5.8×10^{17}	0.58×10^{18}
02	5.8×10^{17}	1.16×10^{18}
03	5.8×10^{17}	1.74×10^{18}
04	5.8×10^{17}	2.32×10^{18}
05	5.8×10^{17}	2.90×10^{18}
06	5.8×10^{17}	3.48×10^{18}
07	5.8×10^{17}	4.06×10^{18}
08	5.8×10^{17}	4.64×10^{18}
09	5.8×10^{17}	5.22×10^{18}
10	5.8×10^{17}	5.80×10^{18}

with argon. The loading chamber was pumped to 10^{-3} Torr, and then a gate valve connecting it with the suitcase was slowly opened to evacuate the nitrogen in the suitcase. After this, the system was pumped down to 1×10^{-7} Torr, and then the cup with the olivine powder was transferred to the main vessel of IGNIS in vacuo using magnetically coupled transfer arms. During the sample preparation and transfer to IGNIS, the olivine powder was never exposed to air.

The ion irradiation was carried out using 1.2 keV He ions from a filament ion source (3 cm FC source, Veeco). The ion energy was selected because it was the maximum energy achievable with the ion sources available in our laboratory. As mentioned in Section 1, laboratory studies of space weathering have often focused on the use of 4 keV He ions. However, the solar wind is not monoenergetic, and the solar wind ions follow an energy distribution (J. T. Gosling 2014). Moreover, it has been shown that the ions can be slowed down or accelerated as they approach Mercury (F. Lavorenti et al. 2023). Thus, studies at different ion energies are important. The ion source used has a beamwidth (FWHM) of 3 cm at the outlet. To monitor the beam current, a titanium disk (10 mm diameter) was placed in the vicinity of the sample. The current measured with this disk was used to estimate the beam flux, assuming singly ionized ions. No secondary electron emission was considered to estimate the flux. To correct for this, a secondary electron emission coefficient (SEEC) of 0.1 was used, based on previous studies from our group (J. P. Allain et al. 2007). The current measured during the irradiation was multiplied by (1-SEEC), and the adjusted current was used to estimate the flux and fluence. A quadratic sum of the uncertainty due to the SEEC and the current variation throughout the experiment were used to estimate the error bars for the fluence reported in this work.

The irradiation was carried out in 10 steps, each with a fluence of $5.8 \times 10^{17} \pm 0.9 \times 10^{17}$ ions cm^{-2}, for a total fluence of $5.80 \times 10^{18} \pm 3.1 \times 10^{17}$ ions cm^{-2}. With an average ion beam flux of 3.92×10^{13} cm^{-2} s^{-1}, each irradiation step took an average of 4 hr and 6 minutes. The flux was monitored during the irradiation, and the standard deviation of the values recorded was used as the flux uncertainty. Propagation of uncertainty was used to estimate the fluence uncertainties, which are used as error bars throughout this document. The irradiation steps are summarized in Table 1. The ion beam flux reported in this work is 5 orders of magnitude higher than the solar wind. However, this is not expected to be an issue for the reasons that are further discussed in Section 4.1.

The sample temperature was not monitored during the irradiation. However, we estimated it to be ~61°C after each 4 hr irradiation step, based on the power delivered by the ion beam and radiative cooling, assuming an initial temperature of 22°C. The real temperature is expected to be lower because conductive cooling was not considered in our estimation. We do not expect the sample temperature to affect the spectral characteristics (R. N. Clark et al. 2011). Moreover, the dark signal was subtracted from each spectral measurement to eliminate any sample emission or background contribution.

UV–Vis–NIR reflectance spectra were measured prior to the initial radiation and after each irradiation step to track the evolution of the spectral properties. Reflectance spectra in the Vis–NIR range (350–2500 nm) were collected with an ASD FieldSpec spectrometer positioned outside of IGNIS. The sample was illuminated with a conventional halogen light bulb placed outside of IGNIS, shining light onto the sample through an optical viewport. The reflected light coming out of a different viewport was focused onto the spectrometer probe using a 90° parabolic mirror placed outside the vacuum chamber. These spectra were collected under a geometry of 14.°9−31.°5−20.°0 incidence–emission–phase angles (*i*–*e*–*g*).

Spectra covering the UV–Vis (200–1100 nm) were collected using an Avantes AvaSpec-ULS2048XL-EVO spectrometer and an Avantes AvaLight-DH-S-BAL deuterium/tungsten lamp for illumination under a 30°−0°−30° (*i*–*e*–*g*) geometry. The spectrometer and lamp were each outside of the chamber and mounted on fiber optics feedthroughs. On the vacuum side, a pair of vacuum-grade fiber optics were mounted on a support bracket and placed ~40 mm away from the sample.

The general arrangement of the instruments is shown in Figure 1(c). A 1″ LabSphere Spectralon disk was used as a reflectance standard for both spectroscopy setups. Reflectance spectra of the olivine powder were recorded before and after each irradiation step, using both instrumental setups. In each case, three spectra were recorded back-to-back, and these were averaged to produce a single spectrum. Spectral reduction and processing were carried out using OriginPro 2021. Corrections for Spectralon were applied using data from the USGS Spectral Library (R. F. Kokaly et al. 2017).

Once the olivine powder was installed inside IGNIS, it was never moved between the irradiation steps and spectral measurements. The sample was kept under high vacuum ($<5 \times 10^{-7}$ Torr) for the entirety of the experiment, except during irradiation, when the pressure increased to 8.8×10^{-4} Torr while the ion gun was backfilled with helium gas (99.999% purity). The gas flow was stopped between the irradiation steps, and the chamber was pumped below 5×10^{-7} Torr while reflectance spectra were collected. As helium gas is inert, we do not expect any reactions with the ion-activated surface during the higher-pressure intervals.

3. Results

3.1. Effects of Ion Irradiation on the Vis–NIR Reflectance

The evolution of the Vis–NIR spectra under 1.2 keV helium ion irradiation of the olivine powder can be seen in Figure 2(a). The spectrum of the pristine olivine powder (step 00) has the general shape of a typical olivine, which is characterized by the presence of a broad absorption feature centered around 1050 nm

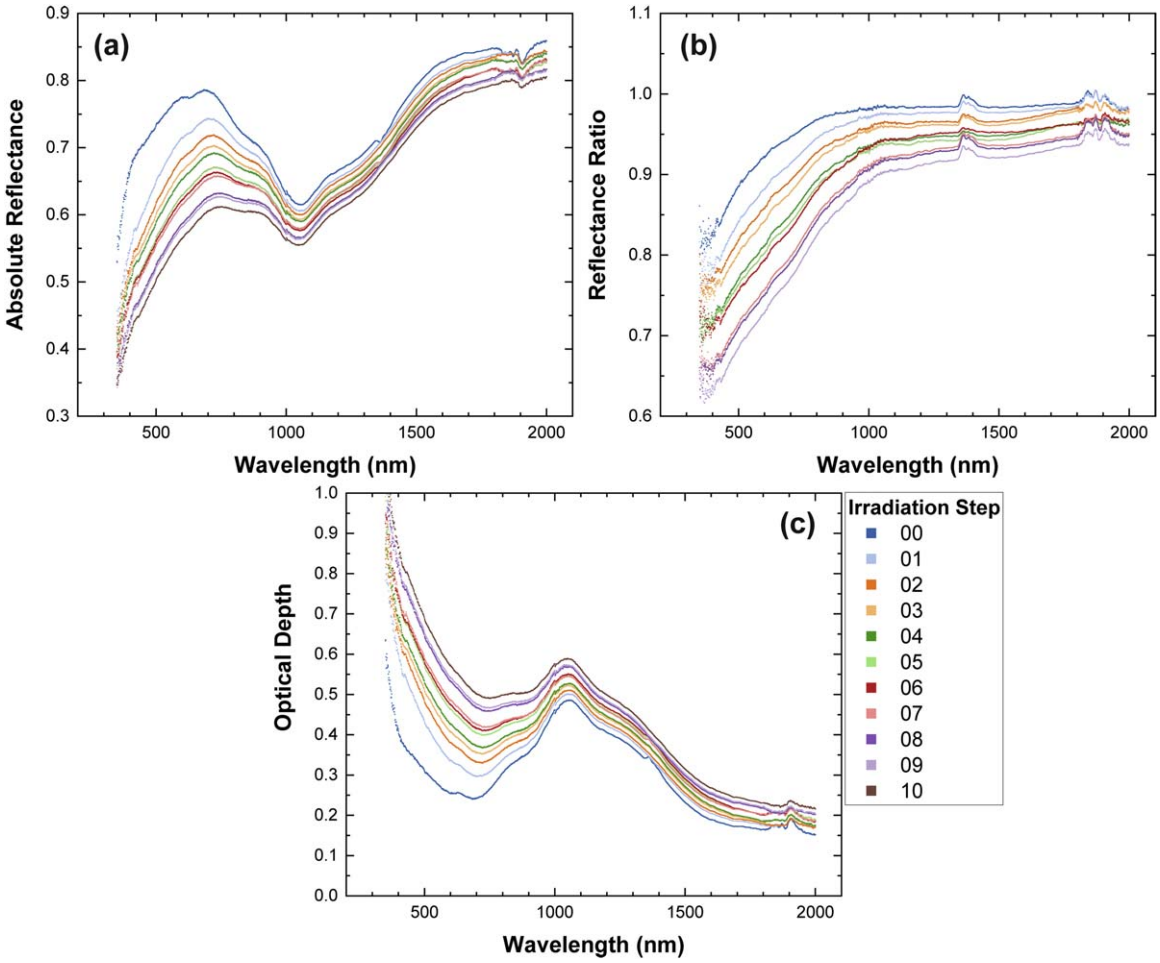

Figure 2. Alteration of the Vis–NIR spectral properties of olivine powder (<25 μm) under 1.2 keV helium ion irradiation. The irradiation was carried out in sequential steps with a fluence of 5.8×10^{17} ions cm^{-2} each, for a total ion fluence of 5.80×10^{18} ions cm^{-2}. (a) Vis–NIR reflectance spectra collected before and after each irradiation step. (b) Reflectance ratios calculated by dividing the reflectance corresponding to each step by the reflectance of the pristine olivine sample (step 00). (c) Optical depth derived from the measured reflectance R given in (a).

(The data used to create this figure are available in the online article.)

attributed to Fe^{2+} in the M2 site. Additional bands observable at 850 and 1250 nm are attributed to Fe^{2+} in the M1 crystallographic coordination site (E. A. Cloutis et al. 2015). The general shape of the olivine spectrum is preserved throughout the ion irradiation. However, alteration of the spectral characteristics is observed beginning with the first irradiation fluence step (at 5.8×10^{17} ions cm^{-2}). The spectral alteration continues throughout the rest of the irradiation fluence.

As can be seen in Figure 2(a), ion irradiation causes a spectral darkening of the reflectance R of the sample. This is more clearly shown in Figure 2(b), where the ratio of the reflectance of irradiated spectra at step n (R_n) to the nonirradiated, initial spectrum (R_0) is plotted as a function of wavelength. In this figure, the spectral darkening continuously increases with increasing ion fluence, up to the maximum fluence evaluated in this study.

The band area was also evaluated, following the procedure described in M. Loeffler et al. (2006) and M. J. Loeffler et al. (2009). Briefly, the optical depth (τ) was obtained from the reflectance R using

$$\tau = \ln(R). \tag{2}$$

The resulting optical depth with each fluence step is shown in Figure 2(c). Next, the area of the optical depth peak corresponding to the 1050 nm absorption band was measured using the Peak Analyzer tool on OriginPro 2021. A baseline of the optical depth across the absorption feature was identified, and then the peak was integrated above this baseline to find its area. The values calculated for the band area after each irradiation step are plotted in Figure 3. The procedure was carried out three times for each spectrum, and the standard deviation of the resulting area in the three iterations is reported as the vertical error bars in this figure. This figure shows that the band area continuously decreases as the total irradiation fluence increases.

The NIR spectral slope of each spectrum was calculated by estimating the slope of a straight line between two points on either side of the 1050 nm absorption band:

$$\text{NIR Slope} = \frac{R_{\lambda_2} - R_{\lambda_1}}{\lambda_2 - \lambda_1}. \tag{3}$$

Using the same wavelength interval used in M. J. Loeffler et al. (2009; i.e., $\lambda_2 = 2000$ nm and $\lambda_1 = 700$ nm), the NIR slope was calculated and plotted (purple squares in Figure 4). The error bars were calculated using propagation of uncertainty of the reflectance spectra, which corresponds to the standard deviation

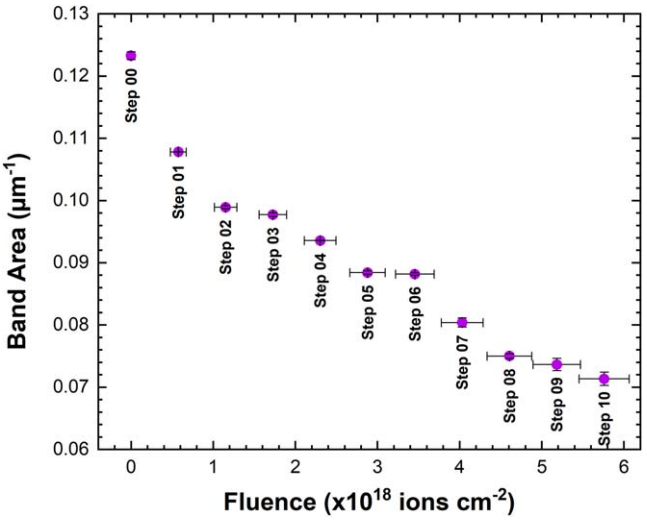

Figure 3. Evolution of the 1050 nm band area of the olivine reflectance spectra as a function of ion fluence.

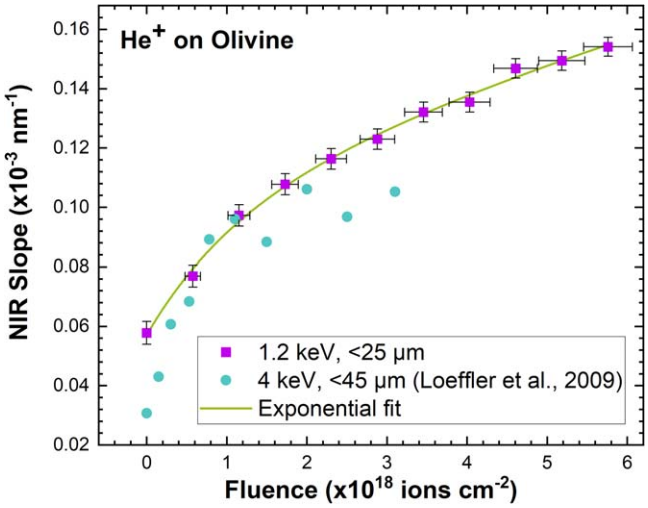

Figure 4. NIR slope of the Vis–NIR reflectance spectra of ion-irradiated olivine powder. The slopes plotted correspond to the slope of a straight line between the reflectance values at 700 and 2000 nm. The purple squares correspond to <25 μm olivine powder irradiated with 1.2 keV helium ions (this work). The blue dots correspond to <45 μm olivine powder irradiated with 4 keV helium ions from M. J. Loeffler et al. (2009). The He ion energy and sample grain size are specified in the legend.

of the three spectra collected before and after each irradiation step. Overall, the NIR slope increases as the irradiation continues.

3.2. Effects of Ion Irradiation on the UV–Vis Reflectance

The UV–Vis spectra of the olivine powder sample, collected between irradiation steps, are shown in Figure 5(a). A light source with a deuterium and halogen lamp was used to illuminate the sample during spectral collection. The emission spectra of these lamps overlap between 500 and 600 nm. This caused increased noise and artifacts in the data collected in this range. Thus, this region was omitted.

Overall, the spectral features characteristic of olivine can be seen. Part of the 1050 nm absorption band (also seen in the Vis–NIR spectra in Figure 2(a)) is observed, although this band extends beyond the wavelength range of the UV–Vis detector used for these measurements. The drop-off toward the UV (below approximately 700 nm) is also observed in the spectra, with reflectance continuously decreasing with decreasing wavelength, which is characteristic of low-iron olivine (E. A. Cloutis et al. 2008). From these curves, the alteration of the UV spectra caused by the ion irradiation can be observed. In general, with increasing ion fluence, the reflectance spectra become darker. The alteration of the spectra can also be seen in the reflectance ratio plot shown in Figure 5(b). Unlike the Vis–NIR case, these are ratios of the spectra of subsequently radiated samples to the spectrum of the initially radiated sample. The unirradiated sample spectrum was disturbed prior to the radiation process, thus presenting a different surface than was irradiated, and thus would contribute differences not solely attributable to the radiation process. Thus, the ratios were calculated by dividing the spectrum corresponding to each step by the spectrum corresponding to the initial step, step 01.

The UV slope of the spectra between 300 and 400 nm was calculated following the same procedure used to calculate the NIR slope (described above) using Equation (3). The slope was calculated in the same wavelength range reported by A. R. Hendrix & F. Vilas (2006). The calculated UV slopes are plotted as a function of their corresponding fluence in Figure 6. Similarly to the Vis–NIR slope, the error bars were calculated with propagation of uncertainty derived from the standard deviation of the spectra collected. As the plot shows, with increasing fluence, the UV slope decreases.

4. Discussion

4.1. Timescales of Spectral Alteration by Solar Wind

Determining the fluences required to produce the observed spectral changes due to solar-wind-driven space weathering is still a matter of debate (B. Hapke 1973; G. Strazzulla et al. 2005; R. Okazaki et al. 2022; N. Takaki et al. 2022). Natural solar-wind-driven mineral alterations occur over timescales of 10^4–10^6 yr (P. Vernazza et al. 2009), which cannot be mimicked in the laboratory. In this work, the ion irradiation was carried out using the maximum flux that could be obtained from our experimental setup ($\sim 4.5 \times 10^{13}$ ion cm^{-2} s^{-1}). This was done to attain sufficiently high fluences to produce measurable space-weathering-like spectral alterations in a reasonable time frame.

Laboratory simulations of space weathering by solar wind ions monitor the amount of weathering as a function of the irradiation fluence. Alterations of the spectral characteristics of the space-weathered materials (minerals and meteorites) have been reported at different fluences, depending on the sample and the experimental conditions. For example, various carbonaceous chondrite (CC) meteorites have exhibited spectral changes due to 40 keV He ion irradiation for fluences as low as 5×10^{15} ions cm^{-2} (R. Brunetto et al. 2014; C. Lantz et al. 2017) and with 40 keV Ar ions at 6×10^{15} ions cm^{-2} (R. Brunetto et al. 2014). Irradiation of an ordinary chondrite with 60 keV Ar ions produced spectral changes at 1.3×10^{15} ions cm^{-2} (G. Strazzulla et al. 2005). Irradiation of CM (Mighei-type CC) and CI (Ivuna-type CC) chondrites at lower energies (20 keV He ions) produced visible changes in the spectra at fluences of 1×10^{16} ions cm^{-2} (T. Nakamura et al. 2019).

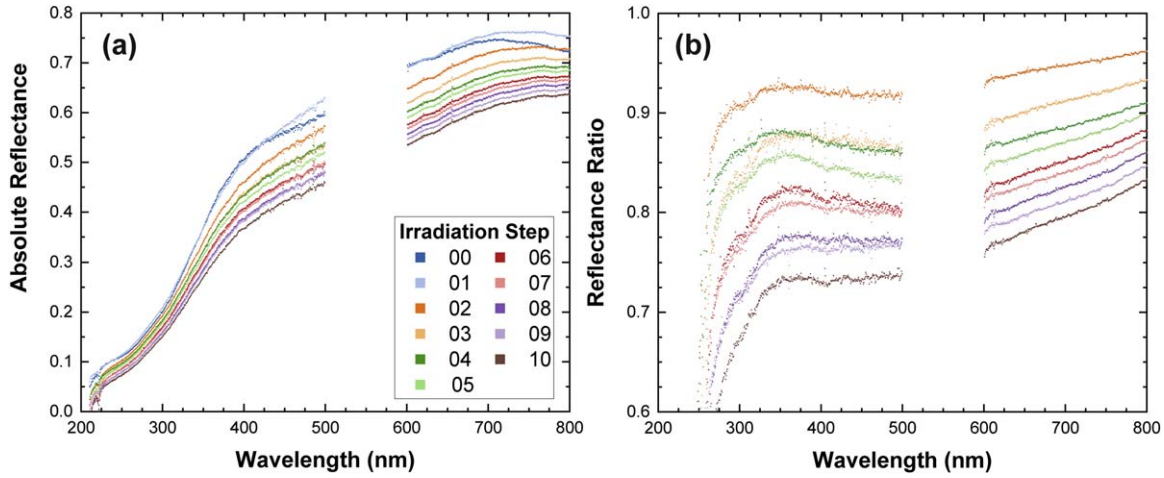

Figure 5. Alteration of the UV–Vis spectral characteristics of olivine powder (<25 μm) by 1.2 keV helium ion irradiation. (a) Absolute reflectance of the mineral recorded at ion fluence intervals of 5.8×10^{17} ions cm^{-2}. (b) Reflectance ratio calculated by dividing the reflectance spectrum of each step by the spectrum corresponding to irradiation step 01. The ratio data in the 500–650 nm range are omitted due to artifacts discussed in the text.
(The data used to create this figure are available in the online article.)

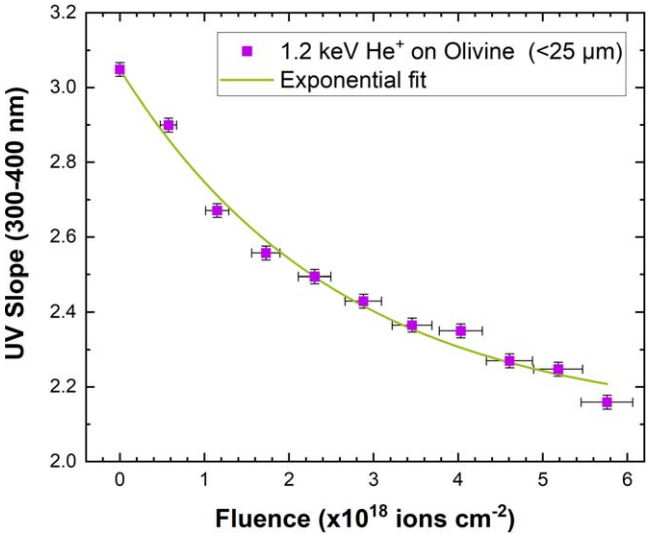

Figure 6. UV slope of the UV–Vis reflectance spectra of ion-irradiated olivine powder. The values plotted correspond to the slope of a straight line between the reflectance at 300 and 400 nm.

At solar-wind-like ion energies, higher fluences are needed to detect spectral alterations. Changes have been observed in the spectra of CCs irradiated with 4 keV He ions at 1×10^{18} ions cm^{-2} (L. P. Keller et al. 2015a). Changes have also been seen in minerals such as anorthite and ilmenite at 1×10^{18} ions cm^{-2} with 1 keV H ions (D. J. Burke et al. 2011), olivine at 1.49×10^{17} cm^{-2} with 4 keV He ions (M. J. Loeffler et al. 2009), and at 5.8×10^{17} ions cm^{-2} with 1.2 keV He ions (this work). Overall, at solar-wind-like ion energies, spectral changes are seen with fluences on the order of $\sim 10^{17}$–10^{18} ions cm^{-2}.

Considering the average solar wind flow speed ($V_{sw} = 468$ km s^{-1}) and particle density at 1 au ($n = 8.7$ ions cm^{-3}), the solar wind flux (ϕ) is given by (J. T. Gosling 2014)

$$\phi = V_{sw} \cdot n = 4.07 \times 10^{8} \text{ ions cm}^{-2}\text{ s}^{-1}. \quad (4)$$

Using the average solar wind flux and our total fluence (Φ) of 5.8×10^{18} ions cm^{-2}, the equivalent exposure time t here at 1 au (assuming constant flux and normal ion incidence) is given by

$$t = \frac{\Phi}{\phi} = 1.26 \times 10^{10}\text{s} \approx 450 \text{ yr}. \quad (5)$$

There is an inherent limitation of laboratory simulations of solar wind ion-driven space weathering. Such simulations must be carried out using laboratory ion beams with fluxes that are orders of magnitude greater than the solar wind flux to achieve measurable effects on the irradiated samples within realistic timescales. Nonetheless, significant results can be produced provided that the laboratory ion irradiation is carried out in such a way that relaxation of any excited electronic states of the irradiated surface can take place. In this work, the irradiations were carried out with an average ion beam flux of 3.92×10^{13} cm^{-2} s^{-1}, which is 5 orders of magnitude larger than the average solar wind estimated in Equation (4). Considering the olivine unit cell dimensions (A. G. Nord et al. 1982) and the atomic arrangement in the unit cell (K. Momma & F. Izumi 2011), the areal atomic density (ρ_a) on the (1 0 0) plane of olivine can be estimated:

$$\rho_a = \frac{8 \text{ atoms}}{10.25\text{Å} \cdot 6.30\text{Å}} = 1.2 \times 10^{15} \text{ atoms cm}^{-2}. \quad (6)$$

This ion beam flux and sample areal density correspond to an atom being impacted by an ion every 3×10^{16} fs. In contrast, electronic relaxation times in solid matter are typically on the order of $\sim 10^{0}$–10^{1} fs (J. I. Mustafa et al. 2016). Specifically, in olivine, electronic thermal stabilization occurs at around 70 fs after high-energy ion bombardment (S. A. Gorbunov et al. 2014). The stark difference between the timescales shows that laboratory simulations occur at rates that allow for electronic relaxation between energy deposition events, even when operating at fluxes that are 5 orders of magnitude larger than the solar wind. Nonetheless, other conditions can affect the fidelity of space weathering laboratory simulations. For instance, while this work was carried out at base pressures of $\sim 1 \times 10^{-7}$ Torr, the solar wind pressure can be roughly estimated as the product of the particle (proton) mass ($m_p = 1.67 \times 10^{15}$ kg), the particle density, and the square of

the flow speed (given above):

$$P = m_p \cdot n \cdot V_{sw} = 2.38 \times 10^{-11} \text{ Torr}. \quad (7)$$

The significantly higher pressure of the laboratory experiment implies that there are more reactive species in the background readily available to interact with the active sites created by the ion irradiation. Moreover, other factors impacting space weathering, such as the dynamic nature of the solar wind, variation in heliocentric distance of the space-weathered bodies, thermal cycles, effects of other space weathering agents such as micrometeorites or cosmic rays, and surface processes like gardening, thermal processing, and comminution (C. M. Pieters & S. K. Noble 2016; J. L. Molaro et al. 2020) may induce different mineral responses that are not driven entirely by the ion irradiation carried out in this laboratory simulation. Thus, the interpretation of the results from laboratory experiments must be done acknowledging this inherent limitation. Nonetheless, laboratory simulations are a useful tool to study space weathering because they enable the study of such processes under controlled environments on humanly viable timescales.

4.2. Spectral Alteration in the Vis–NIR

During our ion irradiation of the olivine powder sample, the evolution of the spectral properties exhibited behavior that has already been linked to space weathering on airless bodies. These include a general spectral darkening in the Vis–NIR, a reduction of the absorption band depth around 1050 nm, and a reddening of the spectra (e.g., D. L. Domingue et al. 2014). These are well-known effects of lunar-style space weathering (M. J. Gaffey 2010).

The impact of solar wind ion bombardment on a powdered mineral has been shown to lead to the formation of rims around the particles, with amorphization of mineral crystals, formation of topographical structures (such as blisters, vesicles, and whiskers), and the appearance of npFe. These phenomena, which have been linked to the spectral alteration, have been observed in laboratory simulations (C. A. Dukes et al. 1999; P. Carrez et al. 2002; M. J. Loeffler et al. 2009; J. M. Young et al. 2019), samples returned from the Moon (L. Gu et al. 2018; L. P. Keller et al. 2021), and samples from asteroids 25143 Itokawa (T. Noguchi et al. 2011, 2014; T. Matsumoto et al. 2020; L. C. Chaves & M. S. Thompson 2022) and 162173 Ryugu (T. Noguchi et al. 2022).

The darkening of the Vis–NIR spectra is observed even at the early stages of our ion irradiation, as seen in Figure 2(a). Reduction of the sample brightness is evident following the initial irradiation step (5.8×10^{17} cm^{-2}). The olivine reflectance at 700 nm—commonly used as a wavelength for spectral analysis (M. Yamada et al. 1999; B. Hapke 2001; S. K. Noble et al. 2007; M. J. Loeffler et al. 2009; D. L. Domingue et al. 2014)—goes from $R_{700-00} = 0.784 \pm 0.004$ on the pristine sample to $R_{700-01} = 0.743 \pm 0.004$ after the first irradiation step, which corresponds to a 5.1% reduction in absolute reflectance. Here the $-xx$ subscript refers to the irradiation step. This reduction of the spectral brightness continues throughout the subsequent irradiation. After a cumulative fluence of 5.80×10^{18} cm^{-2}, the reflectance at 700 nm is $R_{700-10} = 0.606 \pm 0.003$, corresponding to a brightness reduction of 21.8% at 700 nm.

The alteration of the olivine Vis–NIR brightness is, however, wavelength-dependent. The darkening effect is more prominent below 1100 nm, as displayed in Figure 2(b). In the NIR (roughly above 1100 nm), the reflectance ratios show a shallower slope (when compared to the ratio below 1100 nm). The reflectance becomes darker at a faster rate for shorter wavelengths, thus producing an increase in the spectral slope below 1100 nm. This darkening effect has been mainly attributed to the formation of metallic iron in the space-weathered mineral (M. J. Loeffler et al. 2009; D. L. Domingue et al. 2014).

In a different work, 45 μm San Carlos olivine powder was irradiated with 4 keV helium ions (M. J. Loeffler et al. 2009). This corresponds to a slightly higher ion energy than what we report here, although the mineral and ion are the same, and the energy-to-mass ratios are still comparable (i.e., keV light ions impacting on an olivine sample). In Figure 4, we compare the spectral slope of the 1.2 keV He ion-irradiated olivine (this study) with the slope of the 4 keV He ion-irradiated olivine. As the figure shows, the data from both scenarios follow a very similar pattern. In both cases, the evolution of the NIR slope as a function of the fluence follows an exponential trend, with a stronger reddening effect at the early stages of irradiation and less prominent changes in slope as the irradiation continues. Similar trends in the evolution of the spectral slope have been reported before, suggesting a saturation effect (R. Brunetto & G. Strazzulla 2005). A few key differences must be considered when comparing the results from these two reports. TRIM simulations (J. F. Ziegler et al. 2010) were used to estimate the penetration range of He ions impacting on a $Mg_{1.8}Fe_{0.2}SiO_4$ target. An ion range of 10 and 31 nm was calculated for 1 keV and 4 keV He ions, respectively. In terms of the sample grain size, smaller grains produce brighter spectra (T. V. V. King & W. I. Ridley 1987; J. M. Sunshine & C. M. Pieters 1998; E. A. Cloutis et al. 2008). Additionally, smaller grains have more surface area and a higher surface-to-volume ratio. Thus, smaller grains will cause more scattering by photons, leading to more grains encountered. Reflectance spectroscopy of smaller grains will see the effects of surface alteration by ion bombardment sooner than on larger grains. The differences between the two data sets can therefore be attributed to differences in the experimental setup, ion energy, and sample grain size.

Solar-wind-like ion irradiation also alters the characteristics of the olivine Vis–NIR main absorption band located at 1050 nm. Figure 3 shows the band area of the recorded spectra corresponding to each irradiation step. Each irradiation step progressively leads to a shallower absorption band. The band area was reduced by 42% following the final irradiation step.

We also observe a position shift of the features associated with the 1050 nm absorption band. Shifts of the absorption band features caused by ion irradiation of a CC meteorite have been observed before (R. Brunetto et al. 2014). For our studies of ion-irradiated olivine, the position of the shorter-wavelength shoulder and band center were estimated by fitting a parabola to the data with the polynomial fit tool from OriginPro 2021 and then calculating the position of the parabola vertex mathematically. Figure 7(a) shows the absolute wavelength shift of both features, with respect to the feature position on the nonirradiated olivine spectrum. The band center progressively moves toward shorter wavelengths with increasing fluence, whereas the shoulder shifts toward longer wavelengths. As Figure 7(a) shows, the shoulder feature exhibits a more dramatic wavelength shift than the band center. The alteration of the spectra also causes a general albedo reduction, which

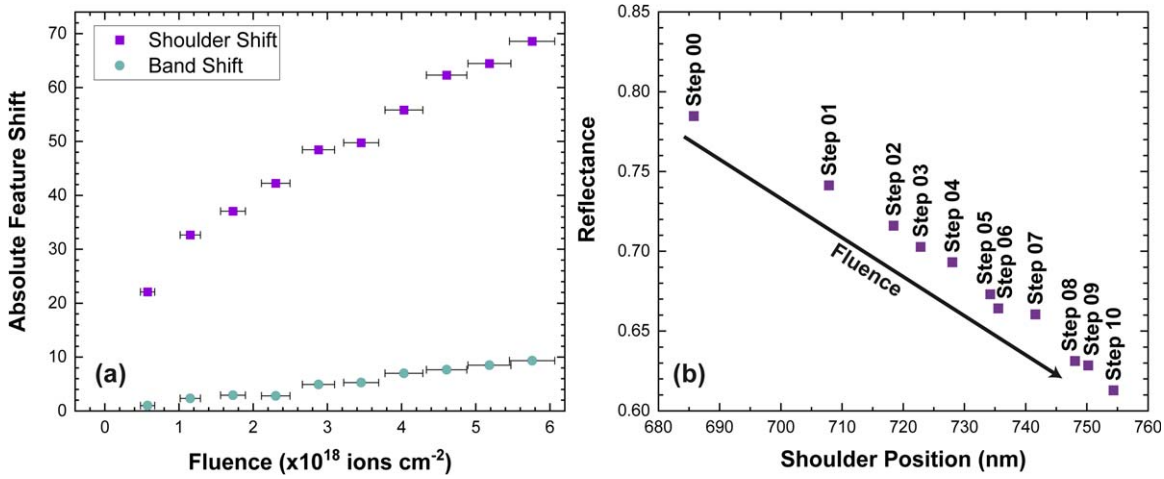

Figure 7. Feature shifting of the olivine absorption band and band shoulder caused by the ion irradiation. (a) Absolute value of the band shoulder and band center shifts with respect to the position on the pristine olivine spectrum. (b) The shoulder shifting is coupled with a reduction of the albedo as the ion fluence increases. The black arrow indicates the direction of increasing fluence.

decreases approximately linearly with the shift of the shoulder (Figure 7(b)).

Overall, the change in the sample brightness, reduction of the 1050 nm absorption band, and increase of the spectral slope take place simultaneously and are evident from the first step. The general trend of each fluence step continues throughout the irradiation process, indicative of the formation of npFe.

4.3. Spectral Alteration in the UV–Vis Wavelength Range

Space weathering has also been linked to alterations in the UV–Vis wavelength region (A. R. Hendrix & F. Vilas 2006, 2019; F. Vilas & A. R. Hendrix 2015). Moreover, it has been suggested that the UV–Vis region is more sensitive to space weathering effects (with respect to the Vis–NIR wavelength range), i.e., the UV–Vis changes occur on shorter timescales (A. R. Hendrix & F. Vilas 2006; F. Vilas & A. R. Hendrix 2015).

In our laboratory-based simulation, the alteration observed in the UV–Vis region is similar to the Vis–NIR in terms of the darkening effect (Figure 5(a)). This spectral darkening is observed from the earliest step of the irradiation, and the sample albedo continues to progressively darken as the fluence increases. The darkening effect is also wavelength-dependent (Figure 5(b)). At longer wavelengths (in the visible and toward the NIR), the reflectance ratio shows a positive slope trend. This indicates that the darkening is less prominent as the wavelength increases (in agreement with the behavior displayed in Figure 2), indicative of a reddening in the spectral properties, as discussed above. At shorter wavelengths (in the near-UV, below ∼400 nm), the reflectance ratios exhibit a decreasing trend, which reflects a bluer spectral slope from the UV–Vis wavelengths.

Figure 6 shows that the spectral slope in the UV (between 300 and 400 nm) decreases as the fluence delivered to the surface of the mineral increases. Similar bluing effects (increasing reflectance with decreasing wavelength) have been reported previously in laboratory simulations and analyses of meteorite samples (Kaňuchová et al. 2010; M. Matsuoka et al. 2015). Although the direction of the slope change is opposite in the Vis–NIR and UV–Vis wavelength regions, both follow an exponential behavior (growth in the case of the former, decay for the latter). This trend in both slope changes suggests there may be a saturation effect that might take place at larger fluences. Such behavior has been linked to an equilibrium of the net ion flux (implanted ion flux equal to resputtered ion species; P. S. Szabo et al. 2020) and saturation of the damage per atom (N. Jaggi et al. 2021). Irradiations at even higher fluences ($>5 \times 10^{18}$ cm^2 s^{-1}) are necessary to evaluate any possible saturation in the mineral response.

4.4. Space Weathering in the UV–Vis versus Vis–NIR

Both the spectral darkening and slope changes in the Vis–NIR and UV–Vis described above have been identified in the comparison of remotely sensed spectra of asteroids (space-weathered surfaces) and laboratory spectra of meteorites (comparable unweathered surfaces; A. R. Hendrix & F. Vilas 2006). Figure 8 shows the slope–slope plot of the Vis–NIR and UV–Vis slopes of different S-class asteroids compared to laboratory data of ordinary chondrites. The arrangement of the spectral data in such slope–slope plots suggests that there is a connection with the exposure age of a surface (related to the amount of space weathering). As Hendrix and Vilas report, most of the meteoritic data—which can be linked to fresher surfaces (i.e., less space-weathered)—exhibit redder (steeper) UV–Vis slopes and bluer (shallower) Vis–NIR slopes, whereas asteroid data—linked to older surfaces (i.e., more space-weathered)—exhibit bluer (shallower) UV–Vis slopes and redder (steeper) Vis–NIR slopes.

The UV and NIR slopes of the 1.2 keV He ion-irradiated olivine powders presented in this work are also plotted in Figure 8. In order to compare our data directly with those of A. R. Hendrix & F. Vilas (2006), our Vis–NIR slopes were recalculated for the 550–1640 nm range. Interestingly, we find a similar correlation in the spectral slope evolution of the olivine powders with ion irradiation as compared to the work of A. R. Hendrix & F. Vilas (2006). The slope–slope values move toward bluer UV and redder NIR regions with weathering, in agreement with the observational and laboratory data reported by A. R. Hendrix & F. Vilas (2006). Moreover, the total slope change observed after each irradiation step was larger in the case of the UV than in the NIR slope (see axis scales in Figure 8), suggesting that the UV wavelength region can be sensitive to smaller changes due to space weathering and exhibit more noticeable spectral changes earlier in the space weathering process.

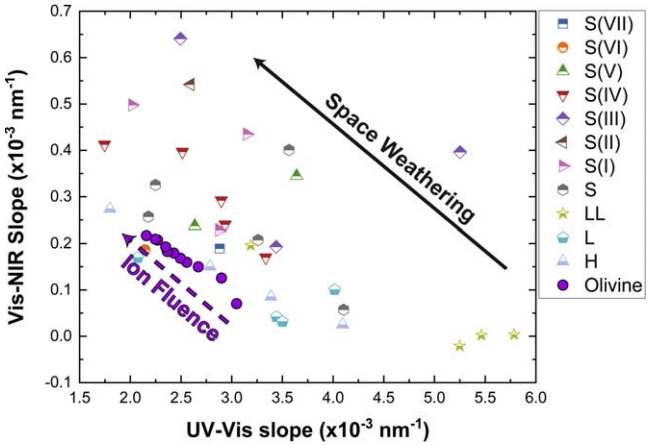

Figure 8. Slope–slope plot of the Vis–NIR slope (550–1640 nm) vs. the UV–Vis slope (300–400 nm) displaying the corresponding slopes of different S-type asteroids and ordinary chondrites (LL, L, and H) as well as the evolution of the spectral slope of the ion-irradiated olivine powders in this work (error bars are within the data points). Asteroid (top-half-filled symbols) and meteorite (bottom-half-filled symbols) data are taken from A. R. Hendrix & F. Vilas (2006). The purple arrow indicates the direction of the spectral slope evolution with increasing ion irradiation fluence reported in this work. The black arrow indicates the general direction of the slope–slope relationship with increasing space weathering timescales proposed by A. R. Hendrix & F. Vilas (2006).

5. Conclusions

Powdered olivine undergoes spectral alteration in the UV–Vis–NIR wavelength range when subjected to irradiation with 1.2 keV helium ions. The simultaneous alteration of the UV–Vis and NIR slopes of terrestrial minerals and meteorites by irradiation with ions of higher energy (>30 keV) has been done before, with spectra collected ex situ (Z. Kaňuchová et al. 2015). To the best of our knowledge, this is the first work to report the spectral alteration of loose olivine powders, tracking the UV–Vis and NIR spectral evolution in situ, when exposed to slow (∼keV) ions simulating solar-wind-driven space weathering. In the Vis–NIR, this transformation is characterized by darkening, reduction of the 1050 nm absorption band, and spectral reddening. Such effects take place progressively as the ion fluence increases. These results are consistent with evidence of space weathering reported in remote observations (B. Hapke 2001; C. R. Chapman 2004; D. L. Domingue et al. 2014; C. M. Pieters & S. K. Noble 2016) and other laboratory simulation studies (R. Brunetto & G. Strazzulla 2005; G. Strazzulla et al. 2005; M. J. Loeffler et al. 2009; Z. Kaňuchová et al. 2010). Additionally, we observed a shifting of the position of the short-wavelength shoulder and band minimum for the 1050 nm band and the band center.

Spectral alteration in the UV–Vis by ion irradiation was also observed. Spectral darkening was observed in this wavelength range, which is consistent with the behavior in the Vis–NIR. However, a decrease of the spectral slope with increasing ion fluence was observed at the shorter wavelengths (below 400 nm). This behavior is in agreement with previous reports (A. R. Hendrix & F. Vilas 2006; F. Vilas & A. R. Hendrix 2015) suggesting that space weathering manifests as a bluing effect in the UV–Vis. Both the UV–Vis and NIR slopes exhibited an exponential trend, hinting at a possible saturation effect. If this prediction is accurate, the slope–slope values in Figure 8 will continue moving along the dashed purple arrow until saturation is achieved, at which point no more changes in the slope–slope values will take place with further ion-driven space weathering. Further studies at even higher fluences are required to verify this prediction.

Further evaluation of the spectral slopes of the laboratory simulations of space-weathered olivine powder reported in this work revealed that the evolution of the Vis–NIR slope with respect to the UV–Vis slope as a function of fluence exhibits a trend similar to observational data of asteroids and meteorites (A. R. Hendrix & F. Vilas 2006): as the mineral is space-weathered, it shifts from steep-UV/shallow-NIR slopes to shallower-UV/steeper-NIR slopes. Our laboratory results support the hypothesis that the correlation of the UV–Vis to Vis–NIR slopes could be an indicator of the degree of space weathering by showing evidence of spectral shifting from steep-UV/shallow-NIR slopes characteristic of fresh surfaces (less space-weathered) to shallow-UV/steep-NIR slopes characteristic of more mature, older surfaces (more space-weathered). This work experimentally establishes a connection between the meteorite (fresh surfaces) and asteroid (older surfaces) data presented by A. R. Hendrix & F. Vilas (2006). Moreover, for the same amount of weathering (or ion fluence), the change in the UV–Vis slope is almost 1 order of magnitude larger than the change in the Vis–NIR slope. This suggests that the UV region could be more sensitive to changes caused by space weathering.

Acknowledgments

The authors thank J. P. Allain for his guidance and contributions that helped the realization of this work. Dr. Allain served as PhD adviser for C.J.-C. while this work was carried out. His contributions earned him a spot as a coauthor of this work. However, he could not be listed as an author due to restrictions related to his employment at the time this manuscript was submitted. The authors thank Prof. M. Sankaran and Q. Cao for sharing their laboratory facilities to carry out this work and C. Bu for stimulating discussions. This work was supported by NASA's Solar System Exploration Research Virtual Institute (SSERVI) Toolbox for Research and Exploration (TREX) grant 80ARC017M0005. D.W.S. and D.D. were supported in part by SSERVI and by NASA's Solar System Workings grant Nos. 80NSCC18K0521 and 80NSCC22K0099.

ORCID iDs

Camilo Jaramillo-Correa https://orcid.org/0000-0003-1181-1733
Neil C. Pearson https://orcid.org/0000-0002-0183-1581
Deborah Domingue https://orcid.org/0000-0002-7594-4634
Daniel W. Savin https://orcid.org/0000-0002-1111-6610
Roger N. Clark https://orcid.org/0000-0002-7021-1220
Faith Vilas https://orcid.org/0000-0003-4723-5870
Amanda R. Hendrix https://orcid.org/0000-0002-0435-8224

References

Allain, J. P., Nieto, M., Hendricks, M. R., et al. 2007, RScI, 78, 113105
Barucci, M. A., Hasselmann, P. H., Fulchignoni, M., et al. 2019, A&A, 629, A13
Bennett, C. J., Pirim, C., & Orlando, T. M. 2013, ChRv, 113, 9086
Blewett, D. T., Denevi, B. W., Cahill, J. T. S., & Klima, R. L. 2021, Icar, 364, 114472
Brunetto, R., Lantz, C., Ledu, D., et al. 2014, Icar, 237, 278
Brunetto, R., & Strazzulla, G. 2005, Icar, 179, 265

Burke, D. J., Dukes, C. A., Kim, J.-H., et al. 2011, Icar, 211, 1082
Carrez, P., Demyk, K., Cordier, P., et al. 2002, M&PS, 37, 1599
Chapman, C. R. 1996, M&PS, 31, 699
Chapman, C. R. 1999, in New Solar System, ed. J. K. Beatty, C. Collins Peterse, & A. Chaikin (4th ed.; Cambridge: Cambridge Univ. Press), 337
Chapman, C. R. 2004, AREPS, 32, 539
Chaves, L. C., & Thompson, M. S. 2022, Earth, Planets and Space, Vol. 74 (SpringerOpen), 124
Clark, B. E., Hapke, B., Pieters, C., & Britt, D. 2002, in Asteroids III, ed. W. F. Bottke et al. (Tucson, AZ: Univ. Arizona Press), 585
Clark, R. N., Pieters, C. M., Green, R. O., Boardman, J. W., & Petro, N. E. 2011, JGRE, 116, E00G16
Cloutis, E. A., Izawa, M. R. M., & Beck, P. 2018, Primitive Meteorites and Asteroids (Amsterdam: Elsevier), 273
Cloutis, E. A., McCormack, K. A., BellIII, J. F., et al. 2008, Icar, 197, 321
Cloutis, E. A., Sanchez, J. A., Reddy, V., et al. 2015, Icar, 252, 39
Demyk, K., Carrez, Ph., Leroux, H., et al. 2001, A&A, 368, L38
Dollfus, A., Wolff, M., Geake, J. E., Lupishko, D. F., & Dougherty, L. M. 1989, in Asteroids II (Tucson, AZ: Univ. Arizona Press), 594
Domingue, D. L., Chapman, C. R., Killen, R. M., et al. 2014, SSRv, 181, 121
Dukes, C. A., Baragiola, R. A., & McFadden, L. A. 1999, JGRE, 104, 1865
Fiege, K., Guglielmino, M., Altobelli, N., et al. 2019, JGRE, 124, 1084
Gaffey, M. J. 2010, Icar, 209, 564
Gaffey, M. J., Bell, J. F., Brown, R. H., et al. 1993, Icar, 106, 573
Gillis-Davis, J. J., Lucey, P. G., Bradley, J. P., et al. 2017, Icar, 286, 1
Goldstein, B. E. 1998, in From the Sun: Auroras, Magnetic Storms, Solar Flares, Cosmic Rays, ed. S. T. Suess & B. T. Tsurutani (Washington, DC: AGU), 73
Gorbunov, S. A., Medvedev, N. A., Rymzhanov, R. A., Terekhin, P. N., & Volkov, A. E. 2014, NIMPB, 326, 163
Gosling, J. T. 2014, Encyclopedia of the Solar System (Amsterdam: Elsevier), 261
Gu, L., Zhang, B., Hu, S., et al. 2018, Icar, 303, 47
Hapke, B. 1973, Moon, 7, 342
Hapke, B. 2001, JGRE, 106, 10039
Hendrix, A. R., & Vilas, F. 2006, AJ, 132, 1396
Hendrix, A. R., & Vilas, F. 2019, GeoRL, 46, 14307
Jaggi, N., Galli, A., Wurz, P., et al. 2021, Icar, 365, 114492
Kaňuchová, Z., Baratta, G. A., Garozzo, M., & Strazzulla, G. 2010, A&A, 517, A60
Kaňuchová, Z., Brunetto, R., Fulvio, D., & Strazzulla, G. 2015, Icar, 258, 289
Keller, L. P., Berger, E. L., Zhang, S., & Christoffersen, R. 2021, M&PS, 56, 1685
Keller, L. P., Christoffersen, R., Dukes, C. A., Baragiola, R. A., & Rahman, Z. 2015a, in Space Weathering of Airless Bodies: An Integration of Remote Sensing Data, Laboratory Experiments and Sample Analysis Workshop (Houston, TX: Lunar and Planetary Inst.), 2010
Keller, L. P., Christoffersen, R., Dukes, C. A., Baragiola, R., & Rahman, Z. 2015b, LPSC, 46, 1913
Keller, L. P., & McKay, D. S. 1993, Sci, 261, 1305
Keller, L. P., & McKay, D. S. 1997, GeCoA, 61, 2331
Keller, L. P., Messenger, S., & Bradley, J. P. 2000, JGRA, 105, 10397
King, T. V. V., & Ridley, W. I. 1987, JGR, 92, 11457
Kokaly, R. F., Clark, R. N., Swayze, G. A., et al. 2017, USGS Spectral Library Version 7, Data Series 1035
Laczniak, D. L., Thompson, M. S., Christoffersen, R., et al. 2021, Icar, 364, 114479
Laczniak, D. L., Thompson, M. S., Dukes, C. A., et al. 2019, LPSC, 50, 1972
Lambart, S., Hamilton, S., & Lang, O. I. 2022, ChGeo, 605, 120968
Lang, E., Kapat, A., & Allain, J. P. 2017, NMEne, 12, 1352
Lantz, C., Brunetto, R., Barucci, M. A., et al. 2017, Icar, 285, 43
Lavorenti, F., Jensen, E. A., Aizawa, S., et al. 2023, PSJ, 4, 163
Loeffler, M. J., Dukes, C. A., & Baragiola, R. A. 2009, JGRE, 114, E03003
Loeffler, M. J., Dukes, C. A., Chang, W. Y., McFadden, L. A., & Baragiola, R. A. 2008, Icar, 195, 622
Loeffler, M., Raut, U., Vidal, R., Baragiola, R., & Carlson, R. 2006, Icar, 180, 265
Lucey, P. G. 2004, GeoRL, 31, L08701
Luo, P., Jaramillo, C., Wallum, A. M., et al. 2020, ACS Appl. Nano Mater., 3, 12025
Matsumoto, T., Harries, D., Langenhorst, F., Miyake, A., & Noguchi, T. 2020, NatCo, 11, 1117
Matsuoka, M., Nakamura, T., Kimura, Y., et al. 2015, Icar, 254, 135
Molaro, J. L., Walsh, K. J., Jawin, E. R., et al. 2020, NatCo, 11, 2913
Momma, K., & Izumi, F. 2011, JApCr, 44, 1272
Mustafa, J. I., Bernardi, M., Neaton, J. B., & Louie, S. G. 2016, PhRevB, 94, 155105
Nakamura, T., Lantz, C., Kobayashi, S., et al. 2019, in 82nd Annual Meeting of The Meteoritical Society, 6211
Noble, S. K., Pieters, C. M., & Keller, L. P. 2007, Icar, 192, 629
Noguchi, T., Kimura, M., Hashimoto, T., et al. 2012, LPSC, 43, 1896
Noguchi, T., Kimura, M., Hashimoto, T., et al. 2014, M&PS, 49, 188
Noguchi, T., Matsumoto, T., Miyake, A., et al. 2022, NatAs, 7, 170
Noguchi, T., Nakamura, T., & Kimura, M. 2011, Science, 333, 1121
Nord, A. G., Annersten, H., & Filippidis, A. 1982, Amerircan Mineralogist, 67, 1206
Okazaki, R., Marty, B., Busemann, H., et al. 2022, Sci, 379, abo0431
Pieters, C. M., & McFadden, L. A. 1994, AREPS, 22, 457
Pieters, C. M., & Noble, S. K. 2016, JGRE, 121, 1865
Pieters, C. M., Taylor, L. A., Noble, S. K., et al. 2000, M&PS, 35, 1101
Price, S. D. 2004, AdSpR, 33, 1548
Strazzulla, G., Dotto, E., Binzel, R., et al. 2005, Icar, 174, 31
sunshine, J. M., & Pieters, C. M. 1998, JGR, 103, 13675
Szabo, P. S., Biber, H., Jaggi, N., et al. 2020, ApJ, 891, 100
Takaki, N., Cho, Y., Morota, T., et al. 2022, Icar, 377, 114911
Thompson, M. S., Morris, R. V., Clemett, S. J., et al. 2020, Icar, 346, 113775
Vernazza, P., Binzel, R. P., Rossi, A., Fulchignoni, M., & Birlan, M. 2009, Natur, 458, 993
Vernazza, P., Fulvio, D., Brunetto, R., et al. 2013, Icar, 225, 517
Vilas, F., & Hendrix, A. R. 2015, AJ, 150, 64
Wentworth, S. J., Keller, L. P., McKay, D. S., & Morris, R. V. 1999, M&PS, 34, 593
Yamada, M., Sasaki, S., Nagahara, H., et al. 1999, EP&S, 51, 1255
Yang, Y., Zhang, H., Wang, Z., et al. 2017, A&A, 597, A50
Young, J. M., Singh, S., Byers, T. A., Jones, D. C., & Rout, B. 2019, NIMPB, 443, 79
Ziegler, J. F., Ziegler, M. D., & Biersack, J. P. 2010, NIMPB, 268, 1818